

## Influence of Thermal Annealing on the Microstructural Properties of Indium Tin Oxide Nanoparticles

Sungnam Kim, Seung Bin Kim,<sup>\*</sup> and Hyun Chul Choi<sup>†,\*</sup>

Department of Chemistry, Pohang University of Science and Technology, Pohang 790-784, Korea. \*E-mail: sbkim@postech.edu

<sup>†</sup>Department of Chemistry and Institute of Basic Science, Chonnam National University, Gwangju 500-757, Korea

\*E-mail: chcl2@chonnam.ac.kr

Received October 10, 2011, Accepted November 19, 2011

In this work, we studied the microstructural changes of ITO during the annealing process. ITO nanoparticles were prepared by the sol-gel method using indium tin hydroxide as the precursor. The prepared sample was investigated using TEM, powder XRD, XPS, DRIFT, and 2D correlation analysis. The O 1s XPS spectra suggested that the microstructural changes during the annealing process are closely correlated with the oxygen sites of the ITO nanoparticles. The temperature-dependent *in situ* DRIFT spectra suggested that In-OH in the terminal sites is firstly decomposed and, then, Sn-O-Sn is produced in the ITO nanoparticles during the thermal annealing process. Based on the 2D correlation analysis, we deduced the following sequence of events: 1483 (due to In-OH bending mode) → 2268, 2164 (due to In-OH stretching mode) → 1546 (due to overtones of Sn-O-Sn modes) → 1412 (due to overtones of Sn-O-Sn modes)  $\text{cm}^{-1}$ .

**Key Words :** ITO nanoparticles, Microstructural changes, Thermal annealing, DRIFT, 2D correlation analysis

### Introduction

Transparent conductive films are used in a variety of electronics and optoelectronics applications, such as solar cells,<sup>1-3</sup> sensors<sup>4-6</sup> and smart windows.<sup>7-9</sup> These films are generally fabricated using metals or wide-band gap oxide semiconductors.<sup>10-12</sup> Among them, tin-doped indium oxide (commonly referred to as ITO) film has attracted particular interest, because of its unique characteristics of high electric conductivity, high luminous transmittance, excellent substrate adhesion, and chemical stability. Crystalline indium oxide ( $\text{In}_2\text{O}_3$ ) possesses a bixbyite structure with a unit cell including 40 atoms and two equivalent cation sites.<sup>13,14</sup> When Sn atoms are doped into  $\text{In}_2\text{O}_3$ , they are considered to substitute for In without inducing any lattice ordering. Due to the difference in the valence states between the  $\text{In}^{3+}$  and  $\text{Sn}^{4+}$  ions, some oxygen sites are not occupied (oxygen vacancies) in the  $\text{In}_2\text{O}_3$  lattice and the  $\text{Sn}^{4+}$  ions act as an *n*-type donor, releasing electrons to the conduction band. Consequently, ITO thin films exhibit high electric conductivity.

ITO thin films are generally prepared by dry processes including vacuum evaporation, DC magnetron sputtering, chemical vapor deposition, electron beam evaporation, spray pyrolysis and laser ablation. Although these techniques can provide high quality ITO films with a well-controlled microstructure, they tend to involve the use of sophisticated reactors or expensive vacuum systems. For these reasons, solution-based wet processes have emerged as a promising alternative method for the fabrication of ITO thin film.<sup>16-20</sup> The solution-based route presents some advantages, such as the possibility of coating on an arbitrary shape or area, high purity, homogeneity, easier control of the doping level,

relatively inexpensive starting materials and simple equipment. However, the electric conductivity of films prepared by the wet process is somewhat lower than that of the films prepared by the dry process, due to their low packing density, even after annealing at high temperatures. To solve this problem, Goebbert *et al.* proposed a new concept based on the use of already fully-densified crystalline ITO nanoparticles dispersed in water or alcohol as the starting material, and the resulting film showed good electrical conductivity.<sup>21,22</sup>

Since the electric conductivity of ITO nanoparticles is strongly dependent on the concentration of oxygen vacancies and the valence state of Sn, investigating the relationship between the microstructural changes and the preparation conditions is very important. Up to now, many researchers have studied the microstructural changes of ITO nanoparticles during the preparation process using various analysis tools.<sup>23-25</sup> However, these reactions are very complicated and are not well understood. In this study, we investigated the microstructural changes of ITO during the annealing process. ITO nanoparticles were prepared by the sol-gel method using indium tin hydroxide as the precursor. To obtain detailed information about the microstructural changes of the ITO nanoparticles, we obtained their temperature-dependent *in situ* diffused reflectance infrared Fourier transform (DRIFT) spectra in the range of 80-360 °C. We also applied 2D correlation analysis to the DRIFT spectra in order to obtain the sequence of spectral events during the annealing process.

### Experimental

According to a previous work,<sup>26</sup> ITO nanoparticles were prepared by the sol-gel method. The starting materials were

nitrate hydrate ( $\text{In}(\text{NO}_3)_3 \cdot x\text{H}_2\text{O}$ , 99.9%, Aldrich) and tin (IV) chloride hydrate ( $\text{SnCl}_4 \cdot 5\text{H}_2\text{O}$ , 98%, Aldrich). All other reagents and solvents were of analytical grade and were used as received. 5 g of  $\text{In}(\text{NO}_3)_3 \cdot x\text{H}_2\text{O}$  and 5 g of  $\text{SnCl}_4 \cdot 5\text{H}_2\text{O}$  were dissolved in 100 mL of de-ionized water and poly ethylene glycol (PEG, MW = 1000) stabilizer was then added to the mixture solution at 60 °C. The ammonia solution was added dropwise to the above mixture solution till the white colored precursor powder appeared. In order to remove the  $\text{Cl}^-$  and  $\text{NH}_4^+$  ions, this precursor was dispersed in de-ionized water and centrifuged at 3000 rpm several times. The final precipitates were dried in a vacuum oven at 50 °C for 4 h to remove the residual water. After drying, the white precursor was thermally oxidized to indium tin oxide (ITO) at 360 °C and then yellow crystalline ITO powders appeared.

The prepared powder samples were characterized by X-ray diffraction (XRD) at room temperature using a Rigaku MAX 2500V X-ray diffractometer with monochromatized  $\text{Cu K}\alpha_1$  radiation ( $\lambda = 1.5405 \text{ \AA}$ ). The size and shape of the samples were examined by scanning electron microscopy (SEM, Philips XL30S FEG) and transmission electron microscopy (TEM, JEOL JEM-1011). The oxidation states of the metal ions were measured by X-ray photoelectron spectroscopy (XPS, ESCA-LAB 250, ThermoVG scientific) in an ultra high vacuum. This system uses a monochromatized  $\text{Al K}\alpha$  (1486.8 eV) source and a spherical section analyzer. For the analysis of the XPS peaks, the C 1s peak position was set to 285 eV and used as an internal reference to locate the other peaks. The *in situ* DRIFT spectra were recorded at a spectral resolution of  $4 \text{ cm}^{-1}$  with an FTIR spectrometer (Bomem, DA8 FTIR Spectrometer) equipped with a liquid nitrogen-cooled MCT detector. The sample and source compartments were evacuated to 0.8 torr. A Harrick Scientific DRIFT accessory, which includes a heating block attachment, was used. For the preparation of the samples used for the DRIFT experiment, ITO and KBr powders were mixed at an ITO content of 1% and finely ground prior to the analysis. The KBr powder was used as a background. All of the diffuse-reflectance FTIR spectra were measured by co-adding 256 scans in the temperature range from 80 to 360 °C at intervals of 40 °C. The samples were heated under nitrogen at a rate of  $10^\circ\text{C} \cdot \text{min}^{-1}$  and kept at elevated temperatures for 30 min before the spectrum was recorded. The reflectance spectra were processed using the Kubelka-Munk transform within the GRAMS software package.

## Results and Discussion

Figure 1 shows the X-ray diffraction patterns of the prepared samples as a function of the annealing temperature. For the precursor powder, the XRD patterns are in good agreement with the standard data of crystalline  $\text{In}(\text{OH})_3$  (JCPDS card no. 85-1338) with a cubic phase, which indicates that the  $\text{Sn}^{4+}$  ions have been doped into the precursors. Below 220 °C, the main XRD patterns of the samples show no noticeable variation. After annealing at 260 °C, however, the XRD patterns change abruptly. The observed patterns are

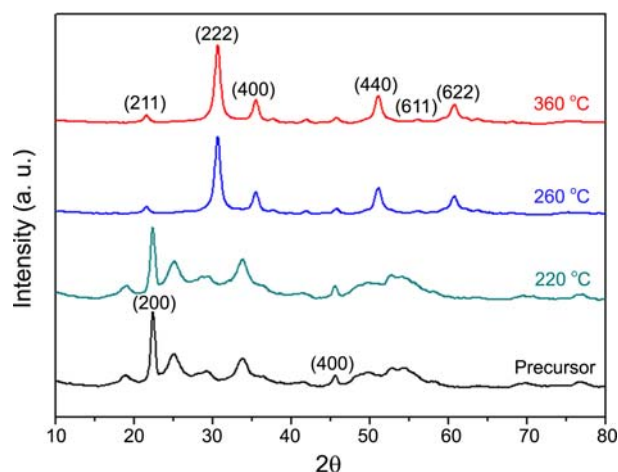
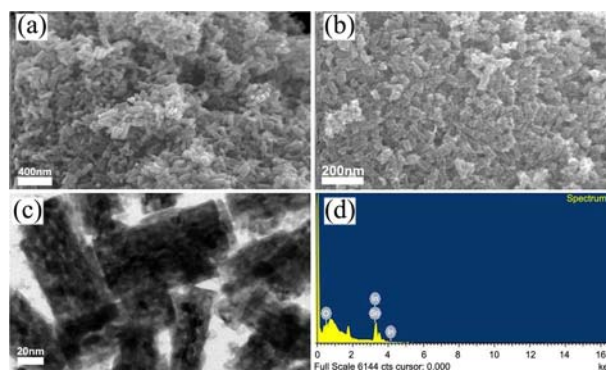


**Figure 1.** X-ray diffraction patterns of samples as a function of annealing temperature.

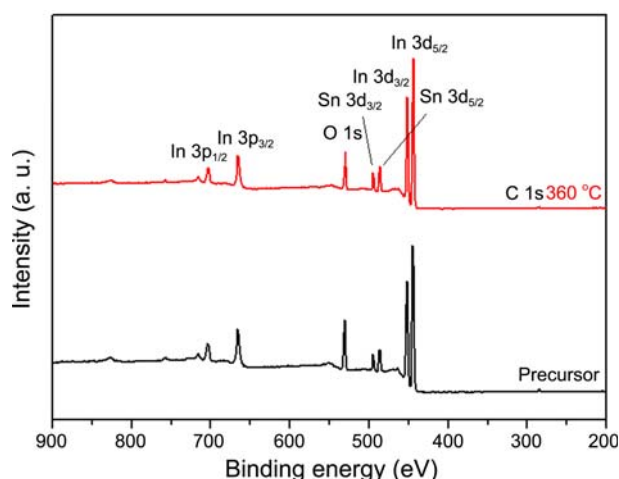
consistent with the standard data of crystalline  $\text{In}_2\text{O}_3$  (JCPDS no. 71-2195) with a cubic phase, which suggests that all of the  $\text{Sn}^{4+}$  ions are dissolved in the  $\text{In}_2\text{O}_3$  matrix and form a single phase of ITO powders. The sharp diffraction peaks indicate that the prepared ITO powders possess high crystallinity. The average particle size of the ITO powder annealed at 360 °C, estimated by applying the Scherrer equation to the (222) diffraction peak, was about 95 nm.<sup>27</sup>

Figure 2 shows a typical SEM image of the precursor and ITO powder annealed at 360 °C. The precursor displays a rectangular morphology with an average particle size of around 80 nm [Figure 2(a)]. For the ITO powder, the SEM and TEM images clearly show that nano-sized rectangular particles were formed [Figure 2(b)-(c)]. Smaller and highly dispersed nanoparticles were much more abundant than larger aggregated ones. The average particle size was estimated to be ~100 nm. This value is in good agreement with that estimated from the XRD peak. The energy dispersive X-ray (EDX) result of the sample implies that the Sn species were incorporated into the  $\text{In}_2\text{O}_3$  matrix [Figure 2(d)].

Figure 3 shows the XPS survey spectra of the precursor and ITO nanoparticles annealed at 360 °C. The XPS results indicated that In, Sn, O and C elements exist on the ITO



**Figure 2.** (a) SEM image of  $\text{In}(\text{OH})_3$  precursors. (b) SEM image of ITO nanoparticles. (c) TEM image of the ITO nanoparticles. (d) EDXS spectrum of ITO nanoparticles.



**Figure 3.** Survey XPS spectra of  $\text{In}(\text{OH})_3$  precursors and ITO nanoparticles.

surface. The detection of C element is related to surface contamination. The relative surface atomic ratio of Sn element was estimated from the corresponding peak areas and corrected with tabulated sensitivity factors. The estimated Sn content was 9.7 atomic %. To elucidate the valence state of the In, Sn and O elements of the ITO nanoparticles annealed at 360 °C, core level XPS analysis was carried out and the result is shown in Figure 4. The core level XPS spectra of the precursor are also shown for comparison. For the ITO nanoparticles, the binding energies (BEs) of a photoelectron in In  $3d_{5/2}$ , In  $3d_{3/2}$ , Sn  $3d_{5/2}$ , and Sn  $3d_{3/2}$  are determined to be 444.1, 451.7, 486.3 and 494.7 eV, respectively. The observed values reveal that the valence states of In and Sn in the sample are mainly +3 and +4, respectively, which are consistent with the previous results.<sup>6,15,28,29</sup> Compared with the precursor, no noticeable change of the XPS signal was observed, except for the slight shift of the In 3d signal due to the microstructural change. However, differences were observed in the O 1s core level XPS spectra after thermal annealing. The O 1s peak (BE = 529.7 eV) was slightly shifted downwards compared to that of the precursor material (BE = 530.8 eV). It is known that the O1s signals of metal ( $\text{Sn}^{4+}$  or  $\text{In}^{3+}$ )-O and metal-OH components of ITO

particles usually appear at  $\sim 530.6$  and  $\sim 532.0$  eV, respectively.<sup>28,29</sup> Therefore, the BE shift of the O 1s peak suggests that the microstructural change during the annealing process mainly occurs around the oxygen sites of the ITO nanoparticles.

Figure 5 shows the temperature-dependent *in situ* DRIFT spectra of the  $\text{In}(\text{OH})_3$  precursor in the temperature range of 80–360 °C. The peak positions and intensities in the DRIFT spectra were found to be quite sensitive to the annealing temperature. Between 2000 and 2500  $\text{cm}^{-1}$ , a broad band is observed at  $\sim 2250$   $\text{cm}^{-1}$  due to the In-OH stretching mode.<sup>30–32</sup> The intensity of this band decreases after annealing and its spectral feature is not observed after annealing at temperatures above 320 °C. Between 2000 and 1750  $\text{cm}^{-1}$ , weak absorption bands at 1943, 1834 and 1770  $\text{cm}^{-1}$  are observed. The bands at 1943 and 1770  $\text{cm}^{-1}$  can be assigned to overtones of the In-O-In modes and the band at 1834  $\text{cm}^{-1}$  is assigned to the In-OH bending modes.<sup>33,34</sup> After annealing, the In-OH bending mode becomes weaker and less structured and the In-O-In overtone modes are detectable in the DRIFT spectra. Below 1750  $\text{cm}^{-1}$ , intense absorption bands at 1546, 1483 and 1411  $\text{cm}^{-1}$  are observed. The two bands at

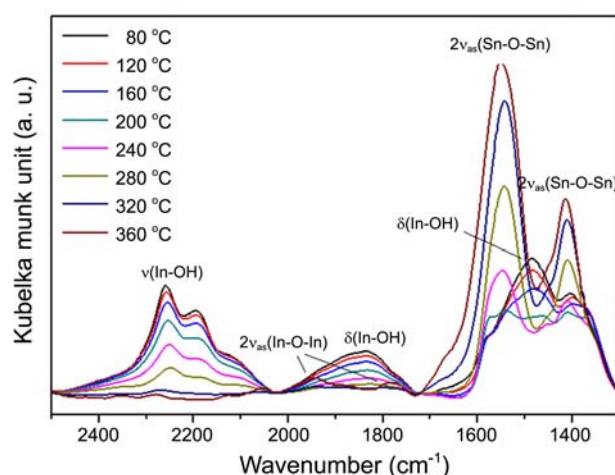


**Figure 5.** Temperature-dependent *in situ* DRIFT spectra of  $\text{In}(\text{OH})_3$  precursors with thermal temperatures in the range from 80 to 360 °C with 40 °C intervals.

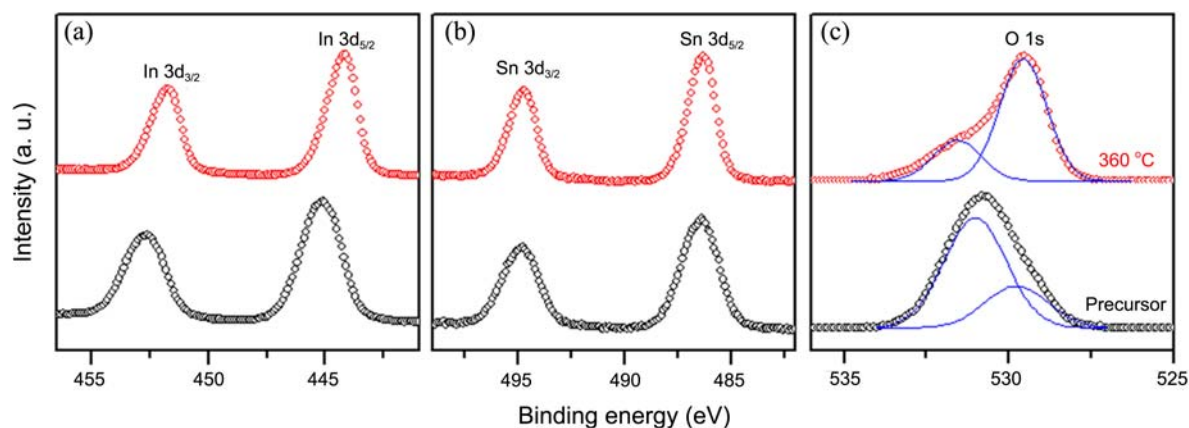


**Figure 4.** Core level XPS spectra of (a) In 3d, (b) Sn 3d, and (c) O 1s photoelectrons. For O 1s signal, the data points (open circles) are fitted by two Voigt profiles (solid lines).

1546 and 1411  $\text{cm}^{-1}$  are assigned to overtones of the Sn-O-Sn modes, while the band at 1483  $\text{cm}^{-1}$  corresponds to the In-OH bending mode.<sup>30-34</sup> It is observed that the former increased and the latter gradually decreased during the annealing process. The observed DRIFT spectra indicate that the Sn-O-Sn component is produced due to the decomposition of the  $\text{In}(\text{OH})_3$  precursor during the thermal annealing.

To determine the sequence of spectral events during the thermal annealing, we applied 2D correlation analysis to obtain the DRIFT spectra. 2D correlation analysis is a technique where the spectral intensity is plotted as a function of two independent spectral variables.<sup>35-37</sup> In a synchronous 2D correlation spectrum, the intensity of the auto peaks located at the diagonal positions represents the overall susceptibility of the corresponding spectral region to changes in the spectral intensity as an external perturbation is applied to the system, while the intensity of the cross-peaks located at the off-diagonal positions of a synchronous 2D correlation spectrum reveal the simultaneous or coincidental changes of the spectral intensities observed at two different spectral variables ( $\nu_1$  and  $\nu_2$ ). In contrast, an asynchronous 2D correlation spectrum consisting of only cross peaks provides useful information to interpret the mechanisms of chemical/physical interactions. The intensity of the asynchronous spectrum represents the sequential or successive changes of the spectral intensities measures at  $\nu_1$  and  $\nu_2$ . An asynchronous cross peak develops only if the changes in the intensities of the two spectral features are out of phase (i.e., delayed or accelerated) with each other. This feature of an asynchron-

ous spectrum is especially useful in enhancing the spectral resolution of highly overlapped bands. If the signs of the synchronous and asynchronous cross peaks are the same, the intensity change at  $\nu_1$  occurs before that at  $\nu_2$ . If the signs of the synchronous and asynchronous cross peaks are different, the intensity change at  $\nu_1$  occurs after that at  $\nu_2$ .

Figures 6(a) and (b) show the synchronous and asynchronous 2D DRIFT correlation spectra, respectively. As shown in the power spectrum extracted along the diagonal line of the synchronous 2D correlation spectrum shown at the top of Figure 6(a), the intensity of the bands at 1414, 1551, 2195, and 2256  $\text{cm}^{-1}$  are markedly changed during the thermal annealing. The analysis of the 2D correlation spectra shows the following sequence of spectral events during the thermal annealing process: 1483 (due to In-OH bending mode)  $\rightarrow$  2268, 2164 (due to In-OH stretching mode)  $\rightarrow$  1546 (due to overtones of Sn-O-Sn modes)  $\rightarrow$  1412 (due to overtones of Sn-O-Sn modes)  $\text{cm}^{-1}$ . This suggests that In-OH in the terminal site is firstly decomposed and, then, Sn-O-Sn is produced in the ITO nanoparticles during the thermal annealing process.

## Conclusion

It is very important to verify the microstructural changes of ITO nanoparticles during the annealing process, because this change is a critical factor among those determining the properties of ITO materials. In this work, we prepared ITO nanoparticles using the sol-gel co-precipitation method. The prepared sample was investigated using TEM, powder XRD

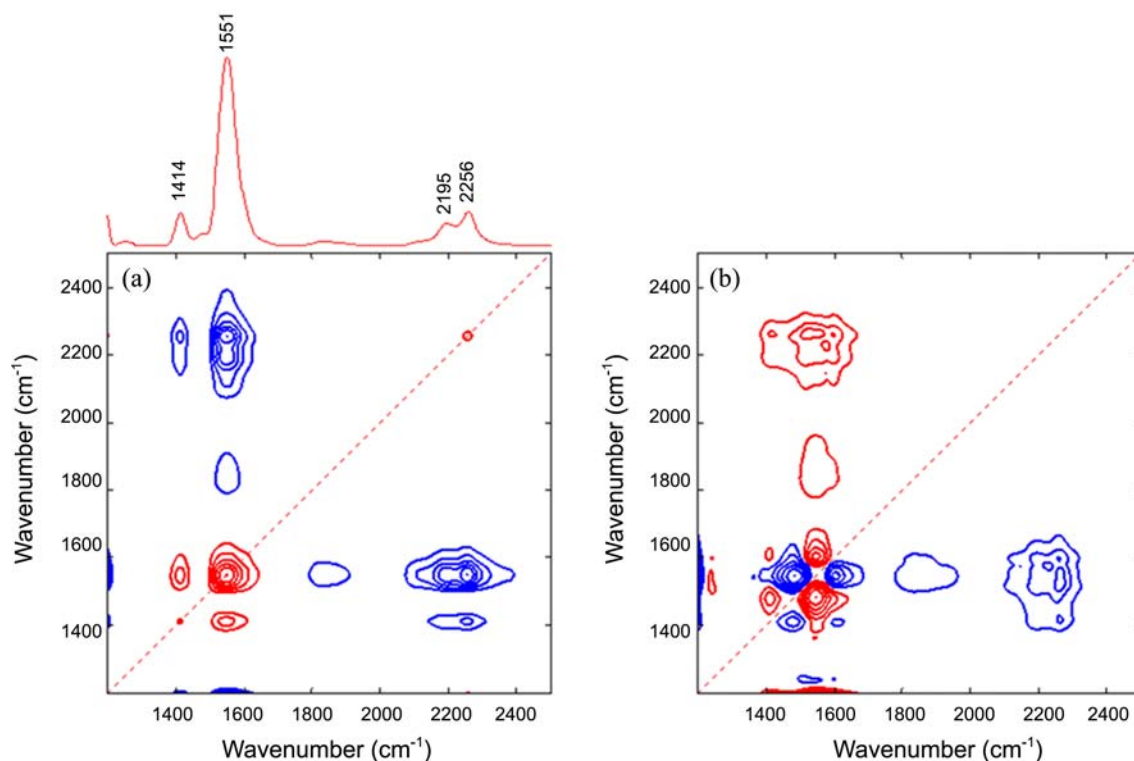


**Figure 6.** (a) Synchronous and (b) asynchronous 2D correlation analysis of the DRIFT spectra obtained from the  $\text{In}(\text{OH})_3$  precursor in the range of 80 to 360  $^{\circ}\text{C}$ . The red and blue lines represent the positive and negative cross peaks, respectively.

and XPS. The TEM images and XRD patterns showed that nano-sized rectangular ITO particles were formed during the annealing process. The average particle size was estimated to be 95 nm. The XPS spectra revealed that the valence states of In and Sn in the sample are mainly +3 and +4, respectively. Furthermore, the BE shift of O 1s suggested that the microstructural change during the annealing process is closely correlated with the oxygen sites of the ITO nanoparticles. From the signs of the cross peaks in the asynchronous 2D correlation spectrum, we deduced the following sequence of spectral events during the annealing process: 1483 (due to In-OH bending mode)  $\rightarrow$  2268, 2164 (due to In-OH stretching mode)  $\rightarrow$  1546 (due to overtones of Sn-O-Sn modes)  $\rightarrow$  1412 (due to overtones of Sn-O-Sn modes)  $\text{cm}^{-1}$ .

**Acknowledgments.** This work was supported by the Second Stage of the Brain Korea 21 Project.

### References

- Hamberg, I.; Granqvist, C. G. *Sol. Energy Mater.* **1986**, *14*, 241.
- Mwamburi, M.; Wakelgad, E.; Roos, A. *Thin Solid Films* **2000**, *374*, 1.
- Granqvist, C. G. *Sol. Energy Mater. Sol. Cells* **2007**, *91*, 1529.
- Jiao, Z.; Wu, M.; Gu, J.; Sun, X. *Sens. Actuator. B* **2003**, *94*, 216.
- Sberveglieri, G.; Benussi, P.; Coccoli, G.; Groppelli, S.; Nelli, P. *Thin Solid Films* **1990**, *186*, 349.
- Xu, J.; Wang, X.; Shen, J. *Sens. and Actuators B* **2006**, *115*, 642.
- Kim, H.; Gilmore, C. M.; Horwitz, J. S.; Pique, A.; Murata, H.; Kushto, G. P.; Schlaf, R.; Kafafi, Z. H.; Chrisey, D. B. *Appl. Phys. Lett.* **2000**, *76*, 259.
- Kim, H.; Pique, A.; Horwitz, J. S.; Mattoussi, H.; Murata, H.; Kafafi, Z. H.; Chrisey, D. B. *Appl. Phys. Lett.* **1999**, *74*, 3444.
- Li, X.; Zhu, Y.; Cai, W.; Borysiak, M.; Han, B.; Chen, D.; Piner, R. D.; Colombo, L.; Ruoff, R. S. *Nano Lett.* **2009**, *9*, 4359.
- Maruyama, T.; Fukui, K. *Thin Solid Films* **1991**, *203*, 297.
- Pearnton, S. J.; Abernathy, C. R.; Overberg, M. E.; Thaler, G. T.; Norton, D. P.; Theodoropoulou, N.; Hebard, A. F.; Park, Y. D.; Ren, F.; Kim, J.; Boatner, L. A. *J. Appl. Phys.* **2003**, *93*, 1.
- Ozgun, U.; Alivov, Y. I.; Liu, C.; Teke, A.; Reshchikov, M. A.; Dogan, S.; Avrutin, V.; Cho, S. J.; Morkoc, H. *J. Appl. Phys.* **2005**, *98*, 041301.
- Nadaud, N.; Lequeux, N.; Nanot, M.; Jov, J.; Roisnel, T. J. *Solid State Chem.* **1998**, *135*, 140.
- Bates, J. L.; Griffin, C. W.; Marchant, D. D.; Garnier, J. E. *Am. Cer. Soc. Bull.* **1986**, *65*, 673.
- Alam, M. J.; Cameron, D. C. *Thin Solid Films* **2000**, *377-378*, 455.
- Pan, Z. W.; Dai, Z. R.; Wang, Z. L. *Science* **2001**, *291*, 1947.
- Al-Dahoudi, N.; Aegerter, M. A. *Thin Solid Films* **2006**, *502*, 193.
- Toki, M.; Aizawa, M. *J. Sol-Gel Sci. Technol.* **1997**, *8*, 717.
- Stoica, T. F.; Stoica, T. A.; Vanca, V.; Lakatos, E.; Zaharescu, M. *Thin Solid Films* **1999**, *348*, 273.
- Sujatha Devi, P.; Chatterjee, M.; Ganguli, D. *Mater. Lett.* **2002**, *55*, 205.
- Goebbert, C.; Nonninger, R.; Aegerter, M. A.; Schmidt, H. *Thin Solid Films* **1999**, *351*, 79.
- Popovi, J.; Gržeta, B.; Tkalec, E.; Tonejc, A.; Bijeli, M.; Goebbert, C. *Mater. Sci. Eng. B* **2011**, *176*, 93.
- Kim, D.; Park, D. *Surf. Coat. Technol.* **2010**, *205*, 5201.
- Xu, B.; Feng, R.; Yang, B.; Deng, Y. *Trans. Nonferrous. Met. Soc. China* **2010**, *20*, 643.
- Cho, H.; Yun, Y. *Ceram. Int.* **2011**, *37*, 615.
- Li, S.; Qiao, X.; Chen, J.; Wang, H.; Jia, F.; Qiu, X. *J. Cryst. Growth* **2006**, *289*, 151.
- Musić, S.; Gotić, M.; Ivanda, M.; Popović, S.; Turković, A.; Trojko, R.; Sekulić, A.; Furić, K. *Mater. Sci. Eng. B* **1997**, *47*, 33.
- Nunes de Carvalho, C.; Botelho do Rego, A. M.; Amaral, A.; Brogueira, P.; Lavareda, G. *Surf. Coat. Technol.* **2000**, *124*, 70.
- Jeon, M.; Kim, M. *Mater. Lett.* **2008**, *62*, 676.
- Nasser, H.; Rédey, Á.; Yuzhakova, T.; Kovács, J. *React. Kinet. Catal. Lett.* **2008**, *94*, 165.
- Amalric-Popescu, D.; Bozon-Verduraz, F. *Catal. Today* **2001**, *70*, 139.
- Wuu, D. S.; Lien, S. Y.; Mao, H. Y.; Wang, J. H.; Wu, B. R.; Yao, P. C.; Hsieh, I. C.; Peng, H. H.; Horng, R. H.; Chuang, Y. C. *Thin Solid Films* **2006**, *501*, 346.
- Ho, W. H.; Yen, S. K. *Thin Solid Films* **2006**, *498*, 80.
- Orel, B.; Lavrencic-Stankgar, U.; Crnjak-Orel, Z.; Bukovec, P.; Kosec, M. *J. Non-Crystalline Solids* **1994**, *167*, 272.
- Jung, Y. M.; Noda, I. *Appl. Spectrosc. Rev.* **2006**, *41*, 515.
- Noda, I.; Ozaki, Y. *Two-Dimensional Correlation Spectroscopy: Applications in Vibrational Spectroscopy*; John Wiley & Sons, Inc.: New York, U.S.A., 2004.
- Noda, I. *Appl. Spectrosc.* **1993**, *47*, 1329.